1   The nature of the proximal volcaniclastic materials from the 2021 eruption Fukutoku-

2   Oka-no-Ba in the Izu-Bonin arc.

3

4   Kenta Yoshida*, Yoshihiko Tamura, Tomoki Sato, Erika Tanaka, Noriko Tada, Morihisa Hamada,
5   Takeshi Hanyu, Qing Chang, Shigeaki Ono
6

7   Research Institute for Marine Geodynamics, Japan Agency for Marine-Earth Science and
8   Technology, Natsushima-cho 2-15, Yokosuka, 237-0061 Japan.
9

10   Correspondence
11   Kenta Yoshida, Natsushima-cho 2-15, Yokosuka, 237-0061 Japan.
12   E-mail: yoshida_ken@jamstec.go.jp
13

18   Conflict of interest disclosure

19   There are no entities or relationship, etc. presenting a potential conflict of interest requiring
20   disclosure in relation to this manuscript.
21

24

25

26   Abstract

27   Fukutoku-Oka-no-Ba is a submarine volcano located at 24°17.1′N/141°28.9′E in the Izu–Bonin–
28   Mariana arc, and is one of the most active volcanoes in Japan. This volcano produced an explosive
29   eruption in August 2021 that generated a large amount of volcaniclastic material, some of which drifted
30   westward to Japan and the coastal area of East Asia as a pumice raft. The pumice clasts that drifted for
31   >1000 km were mostly homogeneous and identical to those produced by past historical eruptions. The
32   clasts have trachytic compositions (SiO_2 = 61-63 mass% and Na_2O+K_2O = 8.6-10.0 mass%) and
33   contain augite, plagioclase, olivine (Mg# ~65), and magnetite, along with a small number of mafic
34   enclaves containing diopside and high-Mg olivine (Mg# ~ 92).

35   We undertook a research cruise to investigate the proximal volcaniclastic materials by dredging.
36   The proximal materials include pumice, weakly vesiculated lapilli, and volcanic rocks, which have
37   trachytic composition (SiO_2 contents up to 64.5 mass%). The main minerals in the proximal material
38   are similar to those in the drift pumice, although remnants of mafic magma do not occur in the SiO_2-
39   rich samples. The compositional variations of the SiO_2-rich proximal samples are due to plagioclase-
40   dominated fractional crystallization, and the higher-SiO_2 samples yielded lower temperature and
41   pressure among the studied samples.

42   The petrographic and geochemical characteristics of the proximal and drift ejecta from Fukutoku-
43   Oka-no-Ba suggest the magma reservoir was stratified into two parts. The lower part experienced
44   magma mixing with a limited volume of mafic magma, whereas the upper part underwent plagioclase-
45   dominated fractional crystallization. The accumulation of differentiated high-SiO_2 magma in the upper
46   part of the magma reservoir might have increased the pressure in the magma conduit, which then
47   exceeded the critical pressure required for an explosive eruption.

48

49   Keywords: Fukutoku-Oka-no-Ba, Izu–Bonin–Mariana arc, phreatomagmatic eruption, drift pumice
50

51   1. Introduction

52   A large volume of pumice clasts was generated by the 2021 eruption of Fukutoku-Oka-no-Ba (FOB)
53   volcano, which is located at 24°17.1′N/141°28.9′E in the Izu–Bonin–Mariana arc (Fig. 1a). This is one
54   of the most active volcanoes in Japan. The pumice clasts drifted and became distributed over a wide
55   area around the islands of Japan and in many places in the East Asia, including Taiwan, Philippines,
56   and Thailand (Yoshida et al., 2022a, b, c). The large amounts of drift pumice filled port areas and
57   hindered vessel navigation, which led to significant economic losses (Maeno et al., 2022; Yoshida et
58   al., 2022a, c; Asami and Takahashi, 2023). The drift pumice is geochemically homogeneous (Yoshida
59   et al., 2022a) and similar to that generated during past eruptions in 1904, 1914, 1986, and 1992 (Tsuya,

60 1937; Yoshida et al., 1987; Kato, 1988; Nakano and Kawanabe, 1992; Sun et al., 1998), although the

61 color and texture of the pumice are variable (Yoshida et al., 2022a). A notable characteristic of the

62 pumice generated by FOB is the minor but common occurrence of black-colored pumice, which

63 consists mainly of transparent brown glass with magnetite nanocrystals (i.e., nanolites) (Yoshida et al.,

64 2022a). Although recent studies have focused on nanolite precipitation and the mechanism of large

65 eruptions (Scarani et al., 2022), the actual processes that trigger eruptions remain unclear (Dubosq et

66 al., 2022). The biotite-bearing hydrous mineral assemblage of nanolite and higher $Fe^{3+}/\Sigma Fe$ ratio of

67 the nanolite-bearing glass than the nanolite-free glass indicate that oxidation due to fluid infiltration

68 induced nanolite-precipitation and subsequent bubble nucleation, which resulted in the explosive

69 eruption (Yoshida et al., 2023).

70   The 2021 eruption of FOB was large enough to be observed by satellite imaging, and the volcanic

71 column reached a height of ~16 km, corresponding to stratospheric level (Maeno et al., 2022; Yoshida

72 et al., 2022a). Based on Himawari-8 satellite images, Maeno et al. (2022) provided a detailed

73 timeseries of the phreatomagmatic eruption from FOB during 13–15 August 2021. The 2021 FOB

74 eruption column consisted of a vapor-rich plume and a small amount of volcaniclastic materials. The

75 pumice contains virtually no hematite nanolites, which indicates that most of the pumice clasts were

76 ejected into water and subsequently floated due to their buoyancy (Maeno et al., 2022; Yoshida et al.,

77 2023). Whether the pumice floated or sunk depended on its microtexture (Mitchell et al., 2021), and

78 the microtexture of the FOB pumice varies widely due to the presence of nanolites (Yoshida et al.,

79 2022a, 2023). The drift pumice sampled on-land only represents the pumice clasts continued to float

80 over a long transport distance (up to 4000 km). Yoshida et al. (2022b, c) noted that the pumice rafts

81 that drifted longer distances tended to comprise smaller clasts with lesser amounts of black pumice

82 that contained larger vesicles.

83   To understand the nature of the 2021 eruption and magmatic system of FOB, it is necessary to

84 investigate the full range of erupted volcaniclastic materials, including those that did not float. As such,

85 we undertook a research cruise using the R/V *Yokosuka* to investigate these deposits. A dredge survey

86 was undertaken inside and outside the submarine caldera to collect fresh rock samples, both with and

87 without significant vesiculation. In this paper, we describe the petrographic and geochemical features

88 of these samples. These new and previously reported data constrain the nature of the magmatic system

89 of FOB, which can be used to predict and mitigate hazards from submarine volcanoes in the far-off

90 sea.

91

92 ## 2. Materials and Methods

93   ### 2.1.   Geological Background and Research Cruise

94 FOB is one of the most southern volcanoes in the Izu–Bonin arc. The volcano is located within a

95   large volcanic complex that extends approximately 15 and 30 km for E–W and N–S direction,
96   respectively (Fig. 1b). The complex comprises the Kita-Fukutoku-Tai volcano, Kita-Fukutoku caldera,
97   and Minami-Ioto volcano (from north to south), and FOB is the central cone of Kita-Fukutoku caldera,
98   which is ~2 km in diameter (Ito et al., 2011). The summit of FOB before the 2021 eruption had an oval
99   shape (elongate NE–SW) and was flat at a depth of ~30 m below sea level (Ito et al., 2011). Seismic
100 and geomagnetic surveys indicate that a low-velocity zone exists to the north of FOB, which can be
101 attributed to the partially molten region of the magma reservoir (Nishizawa et al., 2002; Onodera et
102 al., 2003). The magmatic system of FOB and Kita-Fukutoku caldera are still poorly understood. Based
103 on Nd and Pb isotopic compositions, Sun et al. (1998) suggested that the magma of FOB is distinct
104 from those of the nearby volcanoes of Ioto, but similar to those of the Hiyoshi Volcanic Complex in
105 the northern part of the Mariana arc.

106   The 2021 FOB eruption occurred in the morning of 13 August 2021 and continued to the morning
107 of 16 August (Japan Meteorological Agency, 2021). Underwater sound and infrasound remote
108 observations indicate that the eruption started at 5:55 AM (in Japan Standard Time; Maeno et al., 2022;
109 Metz, 2022).

110   We undertook a geological survey and sampling around FOB during six dredging operations using
111 the R/V *Yokosuka* during cruise YK22-15 from 14 to 27 August 2022. A double-towing dredging
112 system was used (Supplementary Fig. 1). Figure 1b shows the locations of the dredging operations.
113 Given that the cruise was carried out just 1 yr after the explosive eruption, we remained at least two
114 nautical miles (~3.7 km) from the volcanic vent for safety reasons (green circle in Fig. 1b). We consider
115 that the samples collected by the dredges represent the geology of the volcano, although there remains
116 uncertainty as to whether the dredged samples are representative of their specific locations.

117   Three dredges (YK22-15 D03, D05, and D08) targeted the western side of the volcanic vent along
118 the western slope of the caldera. YK22-15 D08 was a continued dredging operation of YK22-15 D03,
119 because the D03 line was cancelled due to stacking of the dredger. YK22-15 D06 targeted the eastern
120 slope of the outer rim of the crater and YK22-15 D07 targeted the outer slope of the topographic high
121 from the rim of the crater. YK22-15 D04 targeted the southern slope of Kita-Fukutoku-Tai. Detailed
122 locations of the dredges are described in the Supplementary Material.
123
124   2.2.   Analytical Methods

125   Mineral and volcanic glass compositions were determined using a field emission gun electron
126 microprobe (EMP) analyzer equipped with five wavelength-dispersive X-ray detectors (JEOL: JXA-
127 8500F) at Japan Agency for Marine-Earth Science and Technology (JAMSTEC; Yokosuka, Japan).
128 Natural and synthetic standards were used to calibrate the quantitative analyses following the
129 procedure of Yoshida et al. (2022a). The analytical conditions were 15 kV and 10 nA for the
130 accelerating voltage and beam current, respectively, except for analyses of olivine. For some olivine

131   grains, we used an accelerating voltage of 20 kV and beam current of 25 nA. The beam diameter was

132   set to 3 μm for minerals and 5 μm for glass. $Fe^{3+}/\Sigma Fe$ values for clinopyroxene were calculated such

133   that the total cations were four on a six-oxygen basis, whereas $Fe^{3+}/\Sigma Fe$ values for magnetite were

134   calculated for $Fe^{2+} + Mg + Mn = 1$ on a four-oxygen basis. All Fe in olivine was assumed to be ferrous.

135   Anorthite, albite, and orthoclase contents of plagioclase were calculated as $Ca/(Ca+Na+K)\times100$,

136    $Na/(Ca+Na+K) \times100$, and $K/(Ca+Na+K) \times100$, respectively.

137   Cathodoluminescence analysis of silica minerals was conducted using a scanning electron

138   microscope (ThermoScientific: Quanta FEG450) equipped with a cathodoluminescence system

139   (Gatan: MonoCL 4) at JAMSTEC.

140   Raman spectra were obtained with a Raman spectrophotometer (RAMANtouch VIS-HP-MAST;

141   Nanophoton) equipped with a 532 nm semiconductor green laser at JAMSTEC. The laser power on

142   the sample surface was 1-2 mW, and data were acquired in 2×20 s cycles to eliminate accidental

143   cosmic rays. The spectrometer was calibrated to the 520.7 cm^{-1} peak of a Si wafer.

144   Whole-rock major element compositions were determined following the methods of Tani et al.

145   (2005) and Sato et al. (2020), by X-ray fluorescence (XRF) spectrometry (Rigaku ZSX Primus II).

146   Prior to analysis, the samples were crushed to pebble size (5–10 mm) and desalinated using hot water

147   (~40 °C) and by boiling in Milli-Q water. Desalinization was checked using a $AgNO_3$ solution and

148   corresponding precipitation of AgCl, so that no precipitation occurs. The desalinized samples were

149   then washed with Milli-Q water and acetone in an ultrasonic bath, and powdered in an agate mortar

150   or with a Multi-beads Shocker pulverizer. Finally, a mixture of 0.4 g of sample powder and 4 g of

151    $Li_2B_4O_7$ was fused and made into glass beads for XRF analysis. Accuracy and reproducibility of the

152   major element data are better than ±1% and ±2 % (relative standard deviations), respectively.

153   We also analyzed the whole-rock trace element compositions by solution inductively coupled

154   plasma-mass spectrometry (ICP-MS; iCAP Qc; ThermoFisher Scientific). The rock powders were

155   digested in HF, HClO4, and HNO3. We also analyzed a reference basalt (JB-2; Jochum et al., 2016),

156   which yielded results that are in good agreement with certified values (Table S1).

157

3. Results

3.1.   Sample descriptions

160   The recovered rock samples were initially described onboard. The samples include gray to brown

161   pumice, black volcanic rock with variable degrees of vesiculation, and tuff. For convenience, we omit

162   the cruise number (YK22-15) and describe the dredge number with the prefix D and the sample

163   number with the prefix R. For example, D03R01 is the first rock sample from dredge number three.

164   The rock samples are generally fresh and without Mn oxide coatings. The pumice clasts are mostly

165   rounded. In contrast, the black volcanic rock samples are angular to subangular, indicating subsequent

166 reworking was insignificant. The samples collected from the western lines (D03, D05, and D08)

167 contain a considerable amount of pumice and angular volcanic rock clasts that are <10 cm in length

168 (Fig. 2a-b). The most common pumice is gray in color, and is similar to those collected as drift pumice

169 (Yoshida et al., 2022a), while some pumice is dark gray to black (Fig. 2c). Although the drift pumice

170 contains black spots including mafic enclaves and plagioclase-dominated crystal clots with nanolite-

171 bearing glass, such features are rare in the dredged samples. Tuff breccia clasts up to 20 cm in size

172 were also recovered. Several black lapilli clasts with a vitreous luster (i.e., obsidian) were also found

173 (Fig. 2d). Based on the deep-sea camera observations, the seafloor around the D08 position was calm

174 and covered with white volcanic ash (Fig. 1c). The dredge D06 was conducted on the southeastern

175 side of the central vent, and sampled black volcanic rocks with variable degrees of vesiculation that

176 were up to 10 cm in size (Fig. 2e). Smaller pumice clasts were also recovered. During dredge D07 on

177 the northeastern slope of the outer caldera rim, an outcrop of black volcanic rocks was observed by

178 the deep-sea camera (Fig. 1d). The volcanic rock sample D07R01 has a pillow-like structure (Fig. 2f),

179 indicative of the subaqueous extrusion. Dredge D07 also recovered large pumice clasts up to 22 cm in

180 length, which have a well-developed tubular texture (Fig. 2g). This texture is referred to as woody

181 pumice, and is considered to form during a submarine eruption (Kato, 1987).

182 Nine representative samples, including volcanic rock and pumice clasts, were selected for

183 petrographic and geochemical investigations.

184

185 ### 3.2. Whole Rock Geochemistry

186 The nine samples have trachytic compositions regardless of their appearance (i.e., glassy volcanic

187 rock/lapilli or pumice; Table 1; Fig. 3a), with higher SiO_2 (63.7–64.4 mass% on an anhydrous basis)

188 and total alkali (Na_2O+K_2O = 10.2–10.4 mass%) contents as compared with the drift pumice (Yoshida

189 et al., 2022a, b), except for one sample (Fig. 3a). The glassy lapilli sample D06R02 was collected from

190 the southeastern slope of the caldera and has a slightly SiO_2-poor composition that overlaps those of

191 the drift pumice. The whole rock major element compositions of the dredged samples and drift pumice

192 define linear trends in Harker diagrams (Figs. 3b–d).

193 Plots of SiO_2 versus selected trace elements are shown in Figures 3e–f. Three drift pumice

194 compositions reported by Yoshida et al. (2022a) are also shown. Zr/Y and La/Sm ratios of the dredged

195 samples are approximately 9.0 and 8.3, respectively, which are higher than those of the drift pumice,

196 except for sample D06R02 (Figs. 3e–f) that has a similar composition as the drift pumice.

197 N-MORB-normalized trace element diagrams show that the studied samples have similar patterns

198 to the drift pumice from the 1986 and 2021 eruptions (Fig. 3g)

199

200 ### 3.3. Petrography and Mineral/Volcanic Glass Chemistry

201 Based on the occurrence of microlites that are visible under an optical microscope, the pumice and

202   volcanic rock samples respectively were subdivided into microlite-rich and microlite-free types (Table
203   1; Figs. 4a–b). Regardless of the appearance of the pumice or volcanic rock, and occurrence of
204   microlites, all the samples contain a similar phenocryst mineral assemblage of clinopyroxene (Cpx),
205   plagioclase (Pl), olivine (Ol), and magnetite (Mag) (Fig. 4b), with minor amounts of apatite occurring
206   as inclusions and a groundmass phase (Fig. 4c). In a few samples, pyrrhotite occurs as inclusions in
207   clinopyroxene and plagioclase. The microlite-rich pumice clast D08R11 contains cristobalite (Crs) in
208   relatively large vesicles (Figs. 4e and 5d).

209   The microlite-free glassy samples (D06R02 and D08R04) contain pale brown groundmass glass
210   (Fig. 4a) that is weakly vesiculated. In contrast, the microlite-rich glassy samples (D03R01, D07R01,
211   D07R05, and D06R01) contain dark brown groundmass glass (Fig. 4b) with abundant microlites of
212   plagioclase and magnetite (Fig. 5a–b). Figure 4b shows that the abundance of microlites is nearly zero
213   in the interstitial glass between the phenocryst minerals. Raman microscopy revealed that the dark
214   brown glass in the microlite-rich samples has a Raman peak of magnetite nanolites at ~670 cm^{-1}, while
215   this peak was not recognized for the pale brown glass in the microlite-free samples (Fig. 4f).

216   The microlite-free pumice sample (D03R03) is gray and has a strongly vesiculated groundmass that
217   consists of colorless glass. The glass surrounding the plagioclase phenocrysts is colorless and nanolite-
218   free (Fig. 4c), while the plagioclase phenocrysts in the drift pumice is commonly associated with
219   nanolite-bearing brown glass, even though the groundmass glass is generally colorless. Figure 4d
220   shows a plagioclase phenocryst in a gray-type drift pumice from the FOB eruption that was collected
221   in Thailand and described by Yoshida et al. (2022b). The nanolite-rich pumice sample (D08R11) has
222   a dusty and highly vesiculated groundmass (Fig. 4e). Although most vesicles are very small (<50 μm),
223   we identified large vesicles (>100 μm) that occasionally contain spherical cristobalite (Fig. 4e).

224   Mafic magma components such as mafic enclaves and Mg-rich olivine (Mg# ~90) were not
225   recognized in the dredged samples.

226   Below, we describe the characteristics of respective minerals and volcanic glass. Representative
227   EMP analyses are shown in Tables 2–4.

228   Plagioclase is the most abundant minerals in the studied samples, and is generally euhedral and up
229   to 5mm in length. Plagioclase generally has a Ca-rich core with $An_{40-49}Ab_{54-48}Or_{4-3}$ and a Ca-poor rim
230   with $An_{30-38}Ab_{56-62}Or_{7-4}$ (Figs. 5a and 6a), which is similar to the core-rim compositions reported for
231   the drift pumice from FOB (Yoshida et al., 2022a). Brown-colored melt inclusions are common, some
232   of which contain optically-visible microlites of magnetite.

233   Clinopyroxene in the studied samples has an almost homogeneous augite composition with Mg#
234   ~80 (Fig. 6b). Samples D06R01 and D07R05 exhibit significant zonation in Fe-Mg ratios, with
235   D07R05 having cores with Mg# = 93 and rims with Mg# = 78, and D06R02 having cores with Mg#
236   = 72 and rims with Mg# = 80 (Figs. 5b & 6b).

237   Olivine in the studied samples exhibits mostly homogeneous with Fo_{62-65}, where olivine in sample

238   D07R01, D07R05, and D08R11 exhibits increase in Fe contents in the outermost rims (Fig. 5c).

239   Magnetite in the studied samples occurs both as inclusions and a groundmass mineral. The

240   magnetite contains considerable amounts of TiO_2 (up to 11 mass%) and Al_2O_3 (up to 3.2 mass%). The

241   MgO content of magnetite is a useful proxy for temperature (Canil and Lacourse, 2020). The X_{Mg-mag}

242   values (Mg/[Mg + ΣFe]) vary among samples, but are mostly $X_{Mg-mag} = 0.06$ (Fig. 6c). D07R01 has

243   the lowest X_{Mg-mag} values for fine-grained magnetite in the groundmass ($X_{Mg-mag} = 0.044–0.048$),

244   whereas the magnetite in Ca-poor rims yielded higher X_{Mg-mag} values of 0.053-0.057 (Fig. 5a). The

245   highest X_{Mg-mag} values were obtained for sample D06R02, which is a microlite-free volcanic rock,

246   with $X_{Mg-mag} = 0.063–0.072$.

247   The presence of cristobalite in sample D08R11 was confirmed by Raman spectroscopy (Fig. 5d).

248   EMP analysis showed the impurity of Al_2O_3 and Na_2O for 1.0 and 0.6 mass%, respectively (Table 4),

249   corresponding to similar molar amounts (~0.0115 on a two-oxygen basis; Table 4). This is indicative

250   of the incorporation of Al and Na as $[AlO_4/Na^+]^0$ (Schipper et al., 2020). Cathodoluminescence

251   imaging of the cristobalite clearly revealed a radial zoning, which is characteristic of chemical vapor

252   deposition (Schipper et al., 2020). The occurrence of cristobalite in sample D08R11 is similar to that

253   of other deep-sea cristobalite occurrences, such as rhyolite in the Havre, Kermadec Arc (Ikegami et

254   al., 2018), and Kikai Caldera, Japan (Hamada et al., 2023).

255   Glass chemistry was also determined by EMP analysis. For the microlite-rich samples, the sites of

256   EMP analyses were carefully determined using backscattered electron images and the results showing

257   the mineral signature were rejected as mixtures. The glass in the dredged samples has relatively high

258   SiO_2 (>65 mass%) and total alkali ($Na_2O+K_2O > 10$ mass%) contents. The glassy lapilli sample

259   (D06R02), with a whole-rock composition similar to those of the previously reported drift pumice data

260   (Fig. 6d) also has a similar glass composition as the drift pumice (Maeno et al., 2022; Yoshida et al.,

261   2022a). The microlite-rich pumice sample (D08R11) has a wide range of SiO_2 contents (64–73 mass%)

262   and exhibits a negative correlation between SiO_2 and $Na_2O + K_2O$ (Fig. 6d). The glass compositions

263   for each sample vary with the whole-rock compositions except for sample D08R11. For example,

264   D07R01 and D07R05 have the most SiO_2-rich compositions (Fig. 6e). We did not find melt inclusions

265   with low SiO_2 contents (<60 mass%) like those reported from the drift pumice.

266   The groundmass glass in sample D08R11 is heterogeneous with respect to halogen contents, and

267   has a lower Cl content (<0.2 mass%) as compared with the other samples (0.3–0.4 mass%; Fig. 6e).

268   The groundmass glass of the eastern dredge samples (D07R01, D07R05, and D06R01) has relatively

269   higher Cl contents (up to 0.4 mass%), whereas samples from the western dredges and sample D06R02

270   have Cl contents of ~0.3 mass%.

271

272   *4. P–T* Estimates

273   Since pressure estimation using the available mineral paragenesis is not easy, Yoshida et al. (2022a)

274   used a machine-learning-based clinopyroxene single mineral geobarometer (Petrelli et al., 2020) for

275   the drift pumice from FOB, and obtained a pressure of ~250 MPa for the magma reservoir. In the

276   present study, we also used the same clinopyroxene geobarometer (Table 3). Most samples consistently

277   yielded pressures range of 215–279 MPa, except for two samples that yielded higher (D03R01 = 388

278   MPa) and lower (D07R01 = 177 MPa) pressures. The cores of zoned clinopyroxene in samples

279   D07R05 and D06R01 yielded higher pressures of 445 and 371 MPa, respectively.

280   Another pressure indicator is the Cl content of groundmass glass. Figure 6e shows that the western

281   samples (D03R01, D03R03, and D08R04) and sample D06R02 have Cl contents of ~0.3 mass%,

282   whereas the eastern samples (D07R01, D07R05, and D06R01) have Cl contents of up to 0.4 mass%.

283   The glass in sample D08R11 has very low Cl contents down to mostly zero. Based on the experimental

284   studies, the maximum Cl solubility in alkaline melts, such as trachyte, exhibits a negative correlation

285   with increasing pressure and is mostly independent of for compositional differences (Signorelli and

286   Carroll, 2002; Balcone-Boissard et al., 2016). A Cl content of 0.4 mass% corresponds to a pressure of

287   <200 MPa, and thus the higher Cl contents of the eastern samples (except for D06R02) can indicate a

288   lower pressure of their equilibration.

289   Temperature conditions can be determined using the magnetite geothermometer (Canil and

290   Lacourse, 2020) where X_{Mg-mag} values can be transformed into temperatures. As shown in Figure 6c,

291   the calculated temperatures for most samples are 920–940 °C, where sample D06R02 yielded higher

292   temperatures of 940–960 °C. Rim compositions of the groundmass magnetite in some samples

293   (D08R11, D07R01, F07R05, and F06R01) yielded temperatures of <900 °C (Fig. 6c). All of these

294   low-temperature samples contain abundant microlites in the groundmass. In sample D07R01,

295   magnetite inclusions in the plagioclase rims yielded X_{Mg-mag} ~ 0.06, corresponding to a temperature of

296   ~925 °C whereas those in the groundmass yielded temperatures of 882–896 °C.

297   Other conventional geothermometers were applied to mineral-melt pairs carefully selected after

298   thinsection observations. The olivine-melt geothermometer (Putirka et al., 2007) was applied to a melt

299   inclusion and surrounding olivine in sample D07R05 and yielded a temperature of 940 °C. The olivine-

300   melt pair in sample D03R01 yielded a higher temperature of 962 °C. The clinopyroxene-melt

301   geothermometer (Neave and Putirka, 2017) was applied to a melt inclusion-clinopyroxene pair in

302   sample D03R01 and yielded a temperature of 981 °C and pressure of 90 MPa. According to Perkins

303   and Vielzeuf (1992), olivine and clinopyroxene compositions can exist in equilibrium, and thus

304   olivine-melt and clinopyroxene-melt pairs might reflect similar conditions in the magma reservoir,

305   although the pressure value obtained from clinopyroxene-melt pair (D03R01) is apparently lower than

306   other estimates. The plagioclase-melt geothermometer (Putirka, 2008) was applied to the plagioclase

307   rims ($An_{31}Ab_{61}Or_8$) and groundmass glass in sample D07D01, and yielded a temperature of 908–

308   964 °C under the assumption of 0–2 mass % of H_2O in melt.

309   In summary, the coarse-grained phenocryst minerals consistently yielded temperatures of 920–

310   980 °C, whereas rims of coarse-grained magnetite and fine-grained magnetite recorded lower

311   temperatures down to 882 °C.

312

313   ## 5. Discussion

314   ### 5.1. The variation of magma composition

315   Bivariate compositional diagrams of the major elements (Figs. 3b–d) show we linear trends in the

316   low- and high-SiO_2 ranges (61.0–63.5 and 63.5–64.5 mass%, respectively). The reported whole-rock

317   compositions of the drift pumice, including past eruptions, are variable and scattered (Fig. 3a), and

318   plot in the low-SiO_2 range. Selected trace element ratios also exhibit differences between low- and

319   high-SiO_2 samples (Fig. 3e-f). We also show the trace element composition of mafic melt inclusions

320   found in olivine and clinopyroxene (Yoshida et al., 2022a). In the magmatic system of FOB, remnants

321   of primitive mafic magma are limitedly recognized, and include mafic melt inclusions (Maeno et al.,

322   2022; Yoshida et al., 2022a), high-Mg olivine (Kato, 1988; Yoshida et al., 2022a, b), and calcic

323   plagioclase (Yoshida et al., 2022a), most of which occur within or are closely associated with black

324   pumice (Yoshida et al., 2022a, b). The lower Zr/Y and La/Sm ratios of the drift pumice (i.e., low-SiO_2

325   range) as compared with the dredged samples (i.e., high-SiO_2 range) can be explained by the effect of

326   the mafic melt component, although the whole-rock compositions show little change. Relatively

327   scattered compositions in the low-SiO_2 range (Fig. 3a) could reflect heterogeneity in the magma

328   reservoir caused by partial mixing with a small amount of mafic component.

329   In contrast, the compositional trends in the higher-SiO_2 range are characterized by moderate changes

330   in all elements and a CaO decrease with increase in SiO_2. We modeled the compositional change from

331   the medium-SiO_2 sample (D08R04) to the highest-SiO_2 sample (D07R05) by assuming fractional

332   crystallization of the minerals in sample D08R04 (Tables 2-4). As a result, the difference between

333   samples D08R04 and D07R05 can be best explained by extraction of 5.6% plagioclase, 0.3%

334   clinopyroxene, 0.2% olivine, and 0.5% magnetite (i.e., fractionation path A in Figs. 3b–d).

335   The model calculations indicate that the FOB magma compositions reflect the occurrence of mixing

336   and fractionating domains. The former domain is characterized by low-SiO_2 compositions partly due

337   to the involvement of a small amount of mafic magma. This domain is heterogeneous which may be

338   due to incomplete mixing. In contrast, the SiO_2-rich samples represent a gradual change due to

339   plagioclase-dominated fractionation. The SiO_2-rich samples contain high-Cl glass (Fig. 6f), which is

340   an indicative of low pressure, and this fractionating domain might represent the upper most part of the

341   magma reservoir that is not mixing with the deeper part of the reservoir.

342

5.2. Implications for the FOB Magmatic System

343

We undertook dredge sampling around the area of FOB, including the outer slope of Kita-Fukutoku caldera (Fig. 1b). Although previous studies reported the drift pumice had a trachytic composition with SiO_2 <~63 mass%, our dredged samples included more SiO_2-rich samples with $SiO_2 > 64$ mass%. Both the SiO_2-rich and -poor samples have high total alkali contents of up to 10.5 mass%, and thus we consider that all these samples represent the magma reservoir of FOB.

The crustal structure beneath FOB was investigated by acoustic and geomagnetic surveys of Nishizawa et al. (2002) and Onodera et al. (2003). The geomagnetic data indicate a low geomagnetic anomaly in the northwestern region of the volcanic vent of FOB. Onodera et al. (2003) interpreted this anomaly to represent partially molten rocks (i.e., the magma reservoir).

The dredge D07 was conducted on the outer slope of Kita-Fukutoku caldera and volcanic rock samples were collected from a seafloor outcrop (Fig. 1d). Although it is unclear whether these samples were generated by the recent volcanic activity of FOB or represent an older volcanic unit of Kita-Fukutoku caldera, a consistent trend including volcaniclastic materials collected from the inside of the caldera indicates that the chemical composition of the D07 samples reflects the endmember characteristics of the current FOB magma reservoir. The samples from D07 have the most SiO_2-rich compositions and lowest temperatures of ~880 °C (Fig. 6c), which can be interpreted to reflect plagioclase-dominated fractional crystallization during cooling.

The pumice sample containing cristobalite (D08R11) possibly represents remnant volcaniclastic material deposited within the conduit, which was ejected during the early stage of the eruption. Cristobalite occurring in vacancies in volcanic rocks are common in submarine volcanoes (e.g., Ikegami et al., 2018; Hamada et al., 2023), as well as in on-land volcanoes (e.g., Schipper et al., 2017). Schipper et al. (2017, 2020) suggested that cristobalite crystallizes by chemical vapor deposition due to the degassing of halogen species (HF and HCl), and provides evidence of shallow and slow cooling typical of a volcanic plug. After the 2021 eruption, FOB exhibited weak degassing activity, which is evident from the bubbles reaching the sea surface above the summit (Fig. 7a). Samples such as D08R11 could have been generated during inter-eruption activity in a blocked volcanic vent.

Consequently, our results for the dredged samples can be summarized as follows (Fig. 7b). The magma reservoir of FOB is heterogeneous and consists of two domains. Most of the volcaniclastic materials ejected by the 2021 FOB eruption (i.e., pumice) were derived from the deeper low-SiO_2 domain. The deeper domain is characterized by the involvement of a small amount of mafic magma, as is evident from some trace elements (Figs. 3e–f), and the limited occurrence of mafic enclaves (Yoshida et al., 2022a) and nanolite-bearing black pumice (Yoshida et al., 2023). The deeper domain has experienced incomplete mixing due to magma convection (Yoshida et al., 2023), resulting in considerable heterogeneity. The shallower part is characterized by higher-SiO_2 contents and lower

378   pressures of <200 MPa, corresponding to a depth of <8 km assuming a crustal density of 2400 kg/m^3.
379   The shallower domain consists of more differentiated magma, indicating the gravity differentiation.
380   The SiO$_2$-rich less-dense magma may have avoided magma convection and mixing with the deeper
381   domain and does not contain mafic magma components. As a result, the whole-rock and melt
382   compositions became more SiO$_2$ rich, and plagioclase became more stable at lower temperatures. This
383   SiO$_2$-rich magma was either ejected with the pumice and sunk immediately after the explosive
384   eruption, or was effusively erupted from a location other than central vent of FOB, such as dredge site
385   D07. The storage of the differentiated high-SiO$_2$ magma in the upper part of the magma reservoir
386   might have plugged the volcanic conduit and increased the pressure, which ultimately led to the high
387   explosivity of the 2021 eruption.
388

Summary

390   Proximal samples of volcaniclastic sediments and volcanic rocks of FOB exhibit differences as
391   compared with drift pumice collected from coastal areas of Japan (i.e., >1000 km from the volcano).
392   The proximal rocks include pumice and volcanic rocks, most of which have higher SiO$_2$ contents
393   (>63.5 mass%) as compared with drift pumice from the 2021 and earlier eruptions (61–63 mass%),
394   although the constituent minerals are the same. Compositional variations of the SiO$_2$-rich proximal
395   samples resulted from plagioclase-dominated fractional crystallization, and the higher-SiO$_2$ samples
396   yielded lower temperatures and pressures. The petrographic and chemical characteristics of the
397   proximal and drifted ejecta from FOB suggest the magma reservoir contains two distinct domains.
398

Supplementary Materials

400   The detailed positions of the dredges, reference standard analysis for the whole-rock trace element
401   composition, and the outline of the dredge procedure are provided in the Supplementary Material.
402

Acknowledgements

411

References

413 Asami, M. & Takahashi, C. (2023) Drift prediction of pyroclasts released through the volcanic activity
414   of Fukutoku-Okanoba into the marine environment. Marine Pollution Bulletin, 186, 114402.

415 Balcone-Boissard, H., Boudon, G., Cioni, R., Webster, J.D., Zdanowicz, G., Orsi, G., Civetta, L.
416   (2016) Chlorine as a geobarometer for alkaline magmas: Evidence from a systematic study of the
417   eruptions of Mount Somma-Vesvius. Scientific Reports, 6:21726

418 Bryan, S.E., Cook, A.G., Evans, J.P., Hebden, K., Hurrey, L., Colls, P., Jell, J.S., Weatherly, D., and
419   Firn, J. (2012) Rapid, long-distance dispersal by pumice rafting. (2012) Plos one, 7, e40583.

420 Canil, D. & Lacourse, T. (2020) Geothermometry using minor and trace elements in igneous and
421   hydrothermal magnetite. Chemical Geology, 541, 119576.

422 Cáceres, F., Wadsworth, F.B., Scheu, B., Colombier, M., Madonna, C., Cimarelli, C., Hess, K.-U.,
423   Kaliwoda, M., Ruthensteiner, B., & Dingwell, D.B. (2020) Can nanolites enhance eruption
424   explosivity? Geology, 48, 997-1001.

425 Cáceres, F., Scheu, B., Hess, K.-U., Cimarelli, C., Vasseur, J., Kaliwoda, M., Dingwell, D.B. (2021)
426   From melt to crystals: The effects of cooling on Fe–Ti oxide nanolites crystallization and melt
427   polymerization at oxidizing conditions. Chemical Geology, 563, 120057.

428 Costa, F. & Chakraborty, S. (2004) Decadal time gaps between mafic intrusion and silicic eruption
429   obtained from chemical zoning patterns in olivine: Earth and Planetary Science Letters, 227, 517–
430   530.

431 Di Genova, D., Sicola, S., Romano, C., Vona, A., Fanara, S., and Spina, L. (2017) Effect of iron and
432   nanolites on Raman spectra of volcanic glasses: A reassessment of existing strategies to estimate
433   the water content. Chemical Geology, 475, 76-86.

434 Di Genova, D., Caracciolo, A., and Kolzenburg, S. (2018) Measureing the degree of "nanolilization"
435   of volcanic glasses: Understanding syn-eruptive processes recorded in melt inclusions. Lithos,
436   318, 209-218.

437 Di Genova, D., Brooker, R.A., Mader, H.M., Drewitt, J.W.E., Longo, A., Deubener, J., Neuvillem D.R.,
438   Fanara, S., Shebanova, O., Anzellini, S., Arzilli, F., Bamber, E.C., Hennet, L., La Spina, G.,
439   Miyajima, N. (2020) In situ observation of nanolite growth in volcanic melt: A driving force for
440   exprosive eruptions. Science Advances, 6, eabb0413.

441 Dubosq, R., Schneider, D.A., Zhou, X., Gault, B., Langelier, B., Pleše, P. (2022) Bubbles and atom
442   clusters in rock melts: A chicken and egg problem. Journal of Volcanology and Geothermal
443   Research, 428, 107574.

444 Geospatial Information Authority of Japan (2021)
445   https://www.gsi.go.jp/uchusokuchi/20210820fukutokuokanoba.html

446   Hamada, M., Hanyu, T., McIntosh, I.M., Tejada, M.L.G., Chang, Q., Kaneko, K., Kimura, J-I.,
447   Kiyosugi, K., Miyazaki, T., Nakaoka, R., Nishimura, K., Sato, T., Seama, N., Suzuki-Kamata, K.,
448   Tanaka, S., Tatsumi, Y., Ueki, K., Vaglarov, B.S., Yoshida, K. (2023) Evolution of magma supply
449   system beneath a submarine lava dome after the 7.3-ka caldera-forming Kikai-Akahoya eruption.
450   Journal   of   Volcanology   and   Geothermal   Research,   107738.
451   https://doi.org/10.1016/j.jvolgeores.2022.107738

452   Ikegamim, F., McPhie, J., Carey, R., Mundana, R., Soule, A., Jutzeler, M. (2018) The eruption of
453   submarine rhyolite lavas and domes in the deep ocean – Havre 2012, Kermadec Arc. Frontiers in
454   Earth Science, 6: 147.

455   Ito, K., Kato, S., Takahashi, M., Saito, A. (2011) Volcanic topography of Fukutoku-Oka-no-ba volcano
456   in Izu-Ogasawara arc after 2010 eruption. Report of Hydrographic and Oceanographic
457   Researches, 47, 9-13.

458   Japan Meteoric Agency (2021) Monthly volcanic activity reports of Fukutoku-oka-no-ba, 2021 August.
459   https://www.data.jma.go.jp/svd/vois/data/tokyo/STOCK/monthly_v-
460   act_doc/tokyo/21m08/331_21m08.pdf (Webpage title was translated by the authors)

461   Jochum, K.P., Weis, U., Schwager, B., Stoll, B., Wilson, S.A., Haug, G.H., Andreae, M.O., Enzweiler,
462   J. (2016) Reference values following ISO guidelines for frequently requested rock reference
463   materials. Geostandards and Geoanalytical Research, 40, 333-350.

464   Kato, Y. (1987) Woody pumice generated with submarine eruption. Journal of the Geological Society
465   of Japan, 93, 11-20.

466   Kato, Y. (1988) Gray pumice drifted from Fukutoku-oka-no-ba to Ryukyu Islands. Bulletin of the
467   Volcanological Society of Japan Series 2, 33, 21-30 (in Japanese).

468   Kimura, J.-I. & Chang, Q. (2012) Origin of suppressed matrix effect for improved analytical
469   performance in determination of major and trace elements in anhydrous silicate samples using
470   200 nm femtosecond laser ablation sector-field inductively coupled plasma mass spectrometry.
471   Journal of Analytical Atomic Spectrometry, 27, 1549-1559.

472   Lafuente B, Downs R T, Yang H, Stone N (2015) The power of databases: the RRUFF project. In:
473   Highlights in Mineralogical Crystallography, T Armbruster and R M Danisi, eds. Berlin,
474   Germany, W. De Gruyter, pp 1-30

475   Metz, D. (2022) Analysis of International Monitoring System hydrophone triplet data: Identifying the
476   August 2021 eruption at Fukutoku-Okanoba, 24.3°N Bonin Arc. Acoustical Science and
477   Technology, 43, 125-128.

478   Mitchell, S.J., Fauria, K., Houghton, B.F., & Carey, R.J. (2021) Sink or float; microtextural controls
479   on the fate of pumice deposition during the 2012 submarine Harve eruption. Bulletin of
480   Volcanology, 83, 80.

481   Mori, S., Yamashita, H., & Goto, M. (1992) Drifted pumices from Ogasawara Arc to the coast of

482   Sagami Bay. Bulletin of the Hiratsuka City Museum, 15, 1-14.

483   Myers, J. & Eugster, H.P. (1983) The system Fe-Si-O: Oxygen buffer calibrations to 1,500 K.
484   Contributions to Mineralogy and Petrology, 82, 75-90.

485   Nakano, S. & Kawanabe, Y. (1992) Pumices drifted to Iriomote Island in 1991. Bulletin of the
486   Volcanological Society of Japan, 37, 95-98 (in Japanese).

487   Neave, D.A., & Putirka, K.D. (2017). A new clinopyroxene-liquid barometer, and implications for
488   magma storage pressures under Icelandic rift zones. American Mineralogist, 102, 777-794.

489   Nishizawa, A., Ono, T., Sakamoto, H., Matsumoto, Y., Otani, Y. (2002) Ocean bottom seismographic
490   observation at Fukutoku-okanoba submarine volcano. Report of Hydrographic Researches, 38,
491   101-123.

492   Onodera, K., Kato, T., Seo, N. (2003) Crustal structure in the vicinities of Fukutoku-okanoba
493   submarine volcano estimated from gravity and magnetic anomalies. Report of Hydrographic and
494   Oceanographic Researches, 39, 23-31.

495   Perkins, D. & Vielzeuf, D. (1977) Experimental investigation of Fe-Mg distribution between olivine
496   and clinopyroxene: Implications for mixing properties of Fe-Mg in clinopyroxene and garnet-
497   clinopyroxene thermometry. American Mineralogist, 77, 774-783.

498   Petrelli, M., Caricchi, L., & Perugini, D. (2020) Machine learning thermo-barometry: Application to
499   clinopyroxene-bearing magmas. Journal of Geophysical Research: Solid Earth, 125,
500   e2020JB020130.

501   Pistone, M., Blundy, J., Brooker, R.A., & EIMF (2017) Water transfer during magma mixing events:
502   Insights into crystal mush rejuvenation and melt extraction process. American Mineralogist, 102,
503   766-776.

504   Putirka, K.D., Perfit, M., Ryerson, F.J., & Jackson, M.G. (2007). Ambient and excess mantle
505   temperatures, olivine thermometry, and active vs. passive upwelling. Chemical Geology, 241,
506   177-206.

507   Putirka, K.D. (2008). Thermometers and barometers for volcanic systems. Reviews in mineralogy and
508   geochemistry, 69, 61-120.

509   Sato, T., Miyazaki, T., Tamura, Y., Gill, J.B., Jutzeler, M., Senda, R., & Kimura, J.-I. The earliest stage
510   of Izu rear-arc volcanism revealed by drilling at Site U1437, International Ocean Discovery
511   Program Expedition 350. Island Arc, 2020, e12340

512   Scarani, A., Zandoná, A., Di Fiore, F., Valdivia, P., Putra, R., Miyajima, N., Bornhöft, H., Vona, A.,
513   Deubener, J., Romano, C., & Di Genova, D. (2022) A chemical threshold controls
514   nanocrystallization and degassing behavior in basalt magmas. Communications Earth &
515   Environment, 3: 284.

516   Schipper, C.I., Mandon, C., Maksimenko, A., Castro, J.M., Conway, C.E., Hauer, P., Kirilova, M., &
517   Kilgour, G. (2017) Vapor-phase cristobalite as a durable indicator of magmatic pore structure and

518   halogen degassing: an example from White Island volcano (New Zealand). Bulletin of
519   Volcanology, 79, 74.

520 Schipper, C.I., Rickard, W.D.A., Reddy, S.M., Saxey, D.W., Castro, J.M., Fougerouse, D., Quadir, Z.,
521   Conway, C., Prior, D.J., and Lilly, K. (2020) Volcanic SiO_2-cristobalite: A natural product of
522   chemical vapor deposition. American Mineralogist, 105, 510–524.

523 Signorelli, S. & Carroll, M.R. (2002) Experimental study of Cl solubility in hydrous alkaline melts:
524   constraints on the theoretical maximum amount of Cl in trachytic and phonolitic melts. Contributions
525   to Mineralogy and Petrology, 143, 209-218.

526 Sun, C.-H. Stern, R., Yoshida, T., & Kimura, J.-I. (1998) Fukutoku-oka-no-ba Volcano: A new
527   perspective on the Alkalic Volcano Province in the Izu-Bonin-Mariana arc. The Island Arc, 7,
528   432-442.

529 Sun, W. & McDonough, W.F. (1989) Chemical and isotopic systematics of oceanic basalts:
530   Implications for mantle composition and processes. Geological Society London Special
531   Publications, 42, 313-345.

532 Tada, N., Nishikawa, H., Ichihara, H., Watanabe Kayama, H., Kuwatani, T. (2021) Drift of an ocean
533   bottom electromagnetometer from the Bonin to Ryukyu Islands: estimation of the path and travel
534   time by numerical tracking experiments. Earth, Planets and Space, 73, 224.

535 Tamura, Y., Yuhara, M., Ishii, T., Irino, N. & Shukuno, H. (2003). Andesites and dacites from Daisen
536   volcano, Japan: partial-to-total remelting of an andesite magma body. Journal of Petrology, 44, 2243-
537   2260.

538 Tamura, Y., Gill, J. B., Tollstrup, D., Kawabata, H., Shukuno, H., Chang, Q., Miyazaki, T., Takahashi, T.,
539   Hirahara, Y., Kodaira, S., Ishizuka, O., Suzuki, T., Kido, Y., Fiske, R. S. & Tatsumi, Y. (2009). Silicic
540   magmas in the Izu-Bonin oceanic arc and implications for crustal evolution. Journal of Petrology, 50,
541   685-723.

542 Tani, K., Kawabata, H., Chang, Q., Sato, K., & Tatsumi, Y. (2005) Quantitative analyses of silicate
543   rock major and trace elements by X-ray fluorescence spectrometer: Evaluation of analytical
544   precision and sample preparation. Frontier Research on Earth Evolution: IFREE Report for 2003-
545   2004 vol. 2.

546 Tsuya, H. (1937) On the volcanics of the Huzi Volcanic zone, with special reference to the geology
547   and petrology of the Idu and Southern Islands. Bulletin of Earthquake Research Institute, 15, 215-
548   357.

549 Viccaro, M., Giuffrida, M., Nicotra, E., & Cristofolini, R. (2016) Timescales of magma storage and
550   migration recorded by olivine crystals in basalts of the March-April 2010 eruption at
551   Eyjafjallajökull volcano, Iceland. American Mineralogist, 101, 222-230.

552 Yoshida, K., Tamura, Y., Sato, T., Hanyu, T., Usui, Y., Chang, Q., & Ono, S. (2022a) Variety of the
553   drift pumice clasts from the 2021 Fukutoku-Oka-no-Ba eruption, Japan. Island Arc, 31, e12441.

554   Yoshida, K., Tamura, Y., Sato, T., Sangmanee, C., Puttapreecha, R., & Ono, S. (2022b) Petrographic
555   characteristics in the pumice clast deposited along the Gulf of Thailand, drifted from Fukutoku-
556   Oka-no-Ba. Geochemical Journal, 56(5), 134-137.

557   Yoshida, K., Maruya, Y., & Kuwatani, T. (2022c) Chocolate-chip cookie-like pumice from the 2021
558   Fukutoku-Oka-no-Ba eruption: views from SNS-related geology. Japanese Magazine of
559   Mineralogical and Petrological Sciences, 51, 220412. (in Japanese with English abstract)

560   Yoshida, K., Miyake, A., Okumura, S.H., Ishibashi, H., Okumura, S., Okamoto, A., Niwa, Y., Kimura,
561   M., Sato, T., Tamura, Y., & Ono, S. (2023) Oxidation-induced nanolite crystallization triggered
562   the   2021   phreatomagmatic   eruption   of   Fukutoku-Oka-no-Ba,   Japan.
563   https://doi.org/10.21203/rs.3.rs-2403668/v1

564   Yoshida, T., Fujiwara, S., & Aoki, K. (1987) Geochemistry of Fukutoku-oka-no-ba submarine volcano,
565   Izu-Ogasawara arc. Research Report of Laboratory of Nuclear Science, Tohoku University, 20,
566   202-215 (in Japanese).

567

568   Figure Captions

569

570   Figure 1. (a-b) Bathymetric maps. (a) Wide-area map showing the distribution of the Izu-Bonin arc.
571   Bathymetric data are from ETOPO1 (doi:10.7289/V5C8276M). (b) Close-up map around FOB
572   that shows the locations of the dredge sites. Bathymetric data were collected during the YK22-
573   15 cruise. The green circle indicates the two-nautical-mile area of prohibited entry due to safety
574   reasons. (c) Sandy seafloor covered with volcanic ash, which was observed during dredge D08
575   on the western slope of FOB. (d) Outcrop of volcanic rock observed during dredge D07 on the
576   northeastern outer slope of Kita-Fukutoku Caldera.

577

578   Figure 2. Photographs of representative hand specimens collected during the cruise. (a) Well-
579   vesiculated pumice, (b) black-colored lapilli, and (c) black-colored pumice collected during
580   dredges D03 and D08 on the western slope of FOB. (d) Lapilli clasts collected during dredge
581   D05 on the northwest of FOB. (e) Weakly vesiculated trachyte clast collected from the
582   southeastern slope of FOB. The white areas are mainly plagioclase. (f) Volcanic rock and (g)
583   well-developed woody pumice collected during dredge D07 on the northeastern outer slope of
584   Kita-Fukutoku caldera.

585

586   Figure 3. (a) Total alkalis versus silica diagram showing the compositions of the dredged samples and
587   literature data. (b-d) Plots of major elements versus SiO_2, which exhibit linear relationships. (e-
588   f) Plots of selected trace element ratios versus SiO_2. Data for pumice from previous eruptions and
589   melt inclusion in the 2021 drift pumice are also shown. (g) Trace element patterns of dredged
590   samples and drift pumice from the 2021 and 1986 eruptions. Compositions were normalized to
591   N-MORB (Sun & McDonough, 1989). Abbreviations: Y22a, Yoshida et al. (2022a); Y22b,
592   Yoshida et al. (2022b); M22, Maeno et al. (2022); K88, Kato (1988); S98, Sun et al. (1998); Y87,
593   Yoshida et al. (1987).

594

595   Figure 4. (a) Photomicrograph of the microlite-free lapilli clast D08R04. The groundmass consists of
596   weakly vesiculated pale brown glass. (b) Microlite-rich lava D07R01 containing magnetite
597   nanolites in the groundmass glass, which was confirmed by Raman spectroscopy. The interstitial
598   glass is generally microlite-free. (c) Cross-polarized light (XPL) and plane-polarized light (PPL)
599   photomicrographs of the pumice clast D03R03 collected from the western slope of FOB. The
600   glass adjacent to the plagioclase phenocryst is colorless and transparent. (d) Photomicrograph of
601   a pumice clast that drifted from FOB to the Gulf of Thailand. The groundmass surrounding the
602   plagioclase phenocryst has a brown color, which is due to magnetite nanolite crystallization. A

603   detailed petrographic description was provided by Yoshida et al. (2022b). (e) Photomicrograph

604   of the weakly vesiculated pumice clast D08R11 that contains phenocrysts of olivine, plagioclase,

605   and magnetite. Spherical cristobalite also occurs in the vesicles. (f) Representative Raman spectra

606   of the colored glass. Although the groundmass glass in D06R02 and D08R04 is pale brown, it

607   does not exhibit a magnetite nanolite peak at 670 cm^{-1}. The brown glass in D07R01 exhibits a

608   nanolite peak in its Raman spectrum.

609

610 Figure 5. (a) Backscattered electron (BSE) image of the plagioclase phenocryst in the microlite-rich

611   volcanic rock clast D07R01. The temperatures calculated based on the $X_{Mg\text{-}mag}$ values of

612   magnetite crystals included in the plagioclase rim are also shown. (b) Zoned clinopyroxene in the

613   microlite-rich volcanic rock clast D07R05. The Mg# value of clinopyroxene in the core and rim,

614   and temperatures calculated from magnetite are also shown. (c) Zoned olivine observed in sample

615   D07R01. Representative Mg# values of the core and rim are also shown. (d) Raman spectrum of

616   cristobalite in sample D08R11. A reference spectrum taken from the RRUFF database (Lafuente

617   et al., 2016) is shown for comparison. (e) BSE image of the microlite-rich pumice clast D08R11,

618   showing a mineral aggregate of plagioclase, clinopyroxene, and magnetite. Temperatures

619   calculated for magnetite are also shown. (f) Cathodoluminescence image of the cristobalite in the

620   boxed area of (e), which has a radial texture.

621

622 Figure 6. (a-b) Ternary compositional diagram for (a) plagioclase and (b) clinopyroxene in the studied

623   samples. (c) $X_{Mg\text{-}mag}$ values of magnetite in the studied samples and the corresponding

624   temperatures calculated following the method of Canil and Lacourse (2020). (d-f) Glass

625   compositions of the studied samples shown in plots of (d) SiO_2-total alkalis, (e) SiO_2-CaO, and

626   (f) halogen contents.

627

628 Figure 7. (a) Photographs of the sea surface above the volcanic vent of FOB taken on 22 August 2022.

629   Floating bubbles were observed. Under the sea surface, the wall of the volcanic vent is visible.

630   (b) Schematic diagram of the FOB magmatic system inferred from results of this study. See the

631   main text for details.

632

633   Tables

634   Table 1. Whole-rock geochemical compositions of the dredged samples, showing the trace element

635   compositions of selected samples.

636

637   Table 2. Representative compositions of plagioclase.

638

639   Table 3. Representative compositions of clinopyroxene and olivine.

640   Footnote: Pressures for clinopyroxene were calculated using the method of on Petrelli et al. (2020).

641

642   Table 4. Representative compositions of magnetite and silica mineral.

Fig. 1

(a)

(b)

(c) Sandy seafloor

(d) outcrop

Fig. 2

Fig. 3

Fig. 4

(a) D08R04 — Microlite-free gm; Pl; Vac; 400 μm; PPL

(b) D07R01 — Microlite-rich gm; Microlite-free domain; Mag; Ol; Pl; Cpx; 800 μm; PPL

(c) D03R03 — Colorless glass; Pl; Vac; Vac; XPL; PPL; 400 μm

(d) Drift pumice — Nanolite-bearing Brown glass around Pl; Vac; Pl; PPL; XPL; 400 μm

(e) D08R11 — Microlite-rich vesiculated groundmass; Vac; Pl; Ol; Mag; Ap; Crs; XPL; PPL; 400 μm

(f) D06R02; Magnetite nanolite (~670 cm⁻¹); D08R04; D07R01; Intensity (a.u.); Raman shift (cm⁻¹)

Fig. 5

(a) D07R01 — Mag (932℃), Cpx, Pl, $An_{31}Ab_{61}Or_{8}$, $An_{48}Ab_{48}Or_{4}$. JEOL COMP 15.0kV ×200 100μm WD11mm

(b) D07R05 — Cpx, Mag (948℃), Mag (915℃), Mg#94, Ap, Mg#79, Cpx. JEOL COMP 15.0kV ×95 100μm WD11mm

(c) D07R01 — groundmass, Ap, Ol, Pl, Mg#63, Mg#59. JEOL COMP 15.0kV ×220 100μm WD11mm

(d) YK22-15 D08R11 Cristobalite, (415), (228), (111), Intensity (a.u.), Cristobalite reference (RRUFF: R060648), Raman shift (cm^{-1})

(e) D08R11 — Crs, Vesicle, Ap, Pl, Mag, 941℃, 911℃, Cpx. JEOL COMP 15.0kV ×75 100μm WD11mm

(f) D08R11 CL — Crs. 12/24/2022 1:35:48 PM, HV 15.00 kV, spot 7.0, pressure 4.48e-4 Pa, mag 2 146 x, mode None, det External, WD 11.6 mm, Quanta, 40 μm

Fig. 6

(a)

(b)

(c)

(d)

(e)

(f)

Fig. 7

(a) Aug. 22

Vent wall

Floating bubbles

(b)

Side vent

Pl-fractionation

<200 MPa
900 ℃

Pl

>200 MPa
950 ℃

Cpx

Ol

Convection
&
Mixing zone

High-Mg Ol

1250 ℃

High-T Mafic magma

Sample No.	Western line							
	D03R01	D03R02	D03R03	D03R04	D04R01	D08R03	D08R04	D08R11
type	lapilli	pumice	pumice	pumice	pumice	lapilli	lapilli	pumice
microlite	rich	-	free	-	-	-	free	rich
in mass%								
SiO_2	63.06	61.33	62.74	61.04	60.43	62.52	62.47	63.02
TiO_2	0.57	0.59	0.58	0.59	0.65	0.59	0.58	0.57
Al_2O_3	16.57	16.43	16.56	16.17	16.74	16.39	16.66	16.51
Fe_2O_3	4.68	5.30	4.74	5.46	6.03	5.17	4.91	4.60
MnO	0.17	0.17	0.17	0.17	0.19	0.17	0.17	0.17
MgO	0.85	1.50	1.02	1.86	1.42	1.04	1.01	0.94
CaO	2.26	3.15	2.42	3.59	3.36	2.40	2.54	2.31
Na_2O	5.04	4.94	5.06	4.76	4.82	4.91	4.95	5.05
K_2O	5.11	4.65	5.02	4.63	4.56	5.14	5.04	5.09
P_2O_5	0.22	0.24	0.23	0.23	0.28	0.24	0.24	0.22
Total	98.52	98.30	98.53	98.48	98.48	98.57	98.57	98.47
LOI	0.82	1.25	1.60	1.47	1.87	0.44	0.47	1.75
in ppm								
Sc	5.765		4.607			3.48	5.078	2.703
Co	5.105		5.44			5.911	6.039	5.104
Ni	0.604		0.85			0.69	0.573	0.532
Cu	15.668		13.926			17.532	23.696	12.898
Rb	102.895		97.786			101.468	97.946	97.351
Sr	381.091		401.854			385.298	432.896	380.95
Y	31.473		30.462			31.749	30.999	30.792
Zr	282.1		266.22			278.422	268.842	255.013
Nb	11.603		11.139			11.44	11.039	11.041
Cs	2.044		1.963			2.018	1.939	1.944
Ba	1628.653		1557.937			1567.935	1571.212	1560.552
La	80.889		77.939			81.187	79.134	78.154
Ce	151.691		145.449			151.712	148.648	146.606
Pr	16.309		15.722			16.416	16.095	15.904
Nd	58.724		56.303			59.309	57.961	57.213
Sm	9.68		9.476			9.809	9.673	9.545
Eu	1.953		1.909			1.982	1.991	1.961
Gd	7.058		6.818			7.292	7.028	6.928

Tb	1.086	1.047		1.098	1.061	1.061
Dy	5.753	5.632		5.912	5.698	5.698
Ho	1.165	1.122		1.179	1.155	1.153
Er	3.585	3.522		3.654	3.602	3.601
Tm	0.539	0.513		0.541	0.517	0.525
Yb	3.684	3.554		3.724	3.594	3.586
Lu	0.568	0.549		0.575	0.557	0.554
Hf	6.868	6.538		6.959	6.678	6.531
Ta	0.525	0.512		0.533	0.515	0.513
Tl	0.237	0.262		0.232	0.22	0.079
Pb	17.641	17.386		17.578	17.279	12.601
Th	21.248	20.221		21.474	20.853	20.767
U	6.108	5.829		6.219	5.97	6.169

NE line				SE line	
D07R01	D07R05	D07R09		D06R01	D06R02
lava	lava	woody pumice		lapilli	lapilli
rich	rich	-		rich	free
63.13	63.27	62.33		62.58	60.70
0.55	0.55	0.55		0.59	0.60
16.47	16.46	16.74		16.50	16.70
4.77	4.67	4.67		5.07	5.85
0.16	0.16	0.16		0.16	0.17
0.95	0.94	1.04		1.04	1.62
2.28	2.26	2.68		2.51	3.53
4.84	4.83	4.90		4.92	4.68
5.31	5.35	5.05		5.13	4.58
0.20	0.20	0.21		0.24	0.26
98.67	98.68	98.34		98.73	98.69
1.03	1.02	2.70		0.63	0.69
3.765	3.171			5.942	5.946
5.951	5.678			6.242	9.864
1.315	1.284			0.745	4.824
22.445	19.442			20.727	34.807
107.589	107.074			103.452	89.679
335.262	340.913			393.279	500.262
31.204	31.177			31.28	29.066
290.57	290.074			284.739	244.3
12.01	12.086			11.762	10.175
2.121	2.108			2.039	1.788
1557.2	1558.452			1584.703	1451.749
81.591	81.026			82.04	75.035
152.237	153.946			154.28	139.477
16.384	16.261			16.438	15.138
58.124	58.206			59.568	55.082
9.644	9.598			9.741	9.201
1.839	1.836			1.947	1.963
6.924	6.942			7.104	6.716

1.067	1.065	1.065	1.017
5.753	5.676	5.743	5.456
1.151	1.151	1.16	1.076
3.641	3.673	3.64	3.37
0.531	0.538	0.531	0.488
3.661	3.704	3.618	3.352
0.576	0.574	0.569	0.523
7.19	7.238	6.956	6.081
0.559	0.552	0.542	0.467
0.279	0.287	0.22	0.212
18.213	18.305	17.404	15.525
22.493	22.578	21.507	18.934
6.494	6.522	6.284	5.538

Sample No	D03R01		D03R03		D08R04		D08R11	
Note	core	rim	core	rim	core	rim	core	rim
SiO_2	56.75	59.50	58.32	59.68	57.83	59.62	56.30	60.19
TiO_2	0.01	0.07	0.07	0.06	0.00	0.02	0.06	0.00
Al_2O_3	26.37	24.83	26.23	24.52	25.58	24.54	26.79	24.25
Cr_2O_3	0.00	0.13	0.00	0.01	0.01	0.00	0.04	0.00
FeO*	0.56	0.61	0.49	0.55	0.48	0.42	0.55	0.54
MnO	0.00	0.00	0.02	0.00	0.02	0.00	0.01	0.08
MgO	0.05	0.05	0.06	0.03	0.03	0.07	0.02	0.02
CaO	8.96	7.23	8.82	7.01	8.58	6.89	10.03	7.08
Na_2O	5.82	6.72	6.17	6.97	6.14	6.78	5.59	6.74
K_2O	0.69	0.97	0.79	1.11	0.75	1.00	0.59	1.17
total								
O	8	8	8	8	8	8	8	8
Si	2.57	2.66	2.60	2.68	2.61	2.68	2.54	2.70
Ti	0.00	0.00	0.00	0.00	0.00	0.00	0.00	0.00
Al	1.41	1.31	1.38	1.30	1.36	1.30	1.43	1.28
Cr	0.00	0.00	0.00	0.00	0.00	0.00	0.00	0.00
Fe^{3+}								
Fe^{2+}	0.02	0.02	0.02	0.02	0.02	0.02	0.02	0.02
Mn	0.00	0.00	0.00	0.00	0.00	0.00	0.00	0.00
Mg	0.00	0.00	0.00	0.00	0.00	0.00	0.00	0.00
Ca	0.44	0.35	0.42	0.34	0.42	0.33	0.49	0.34
Na	0.51	0.58	0.53	0.61	0.54	0.59	0.49	0.59
K	0.04	0.06	0.04	0.06	0.04	0.06	0.03	0.07
An	44	35	42	33	42	34	48	34
Ab	52	59	53	60	54	60	49	59
Or	4	6	4	6	4	6	3	7

| D07R01 | | D07R05 | | D06R01 | | D06R02 | |
core	rim	core	rim	core	rim	core	rim
56.48	60.24	58.32	60.40	57.86	57.99	56.52	58.64
0.05	0.08	0.04	0.04	0.00	0.07	0.06	0.04
26.72	24.32	25.45	24.48	26.40	25.11	25.85	24.31
0.05	0.00	0.00	0.00	0.00	0.00	0.03	0.04
0.58	0.60	0.48	0.45	0.48	0.48	0.70	0.62
0.00	0.05	0.04	0.00	0.01	0.09	0.05	0.00
0.04	0.06	0.06	0.01	0.08	0.04	0.02	0.04
9.88	6.33	8.20	6.64	9.09	7.92	9.47	7.52
5.47	6.88	6.35	7.11	5.95	6.56	6.06	6.69
0.53	1.25	0.88	1.35	0.81	0.92	0.78	1.02
8	8	8	8	8	8	8	8
2.55	2.70	2.63	2.69	2.59	2.63	2.56	2.66
0.00	0.00	0.00	0.00	0.00	0.00	0.00	0.00
1.42	1.28	1.35	1.29	1.39	1.34	1.38	1.30
0.00	0.00	0.00	0.00	0.00	0.00	0.00	0.00
0.02	0.02	0.02	0.02	0.02	0.02	0.03	0.02
0.00	0.00	0.00	0.00	0.00	0.00	0.00	0.00
0.00	0.00	0.00	0.00	0.01	0.00	0.00	0.00
0.48	0.30	0.40	0.32	0.44	0.38	0.46	0.37
0.48	0.60	0.55	0.61	0.52	0.58	0.53	0.59
0.03	0.07	0.05	0.08	0.05	0.05	0.05	0.06
48	31	40	31	44	38	44	36
48	61	55	61	52	57	51	58
3	7	5	8	5	5	4	6

Sample No	D03R01	D03R03	D08R04	D08R11	D07R01	D07R05		D06R01
Note						core	rim	core
SiO_2	52.66	52.58	52.65	52.65	52.42	53.39	53.00	53.42
TiO_2	0.38	0.39	0.36	0.34	0.40	0.19	0.38	0.18
Al_2O_3	0.64	1.48	0.67	1.82	0.85	1.68	1.22	0.93
Cr_2O_3	0.02	0.10	0.00	0.00	0.05	0.09	0.07	0.02
FeO*	9.43	9.09	9.61	8.79	9.10	4.13	9.62	11.45
MnO	0.19	0.99	0.11	0.68	0.13	0.12	0.79	1.07
MgO	15.36	15.35	15.21	15.44	15.45	17.50	15.26	14.19
CaO	19.88	20.22	20.16	20.53	20.19	23.32	20.59	19.88
Na_2O	0.45	0.38	0.48	0.38	0.41	0.22	0.45	0.46
K_2O	0.01	0.01	0.00	0.00	0.00	0.00	0.00	0.00
total	99.03	100.59	99.23	100.63	99.00	100.63	101.37	101.59
O	6	6	6	6	6	6	6	6
Si	1.97	1.94	1.97	1.94	1.96	1.93	1.94	1.97
Ti	0.01	0.01	0.01	0.01	0.01	0.01	0.01	0.00
Al	0.03	0.06	0.03	0.08	0.04	0.07	0.05	0.04
Cr	0.00	0.00	0.00	0.00	0.00	0.00	0.00	0.00
Fe^{3+}	0.04	0.06	0.05	0.06	0.05	0.07	0.07	0.04
Fe^{2+}	0.25	0.22	0.25	0.21	0.24	0.06	0.22	0.31
Mn	0.01	0.03	0.00	0.02	0.00	0.00	0.02	0.03
Mg	0.86	0.84	0.85	0.85	0.86	0.94	0.83	0.78
Ca	0.80	0.80	0.81	0.81	0.81	0.90	0.81	0.79
Na	0.03	0.03	0.03	0.03	0.03	0.02	0.03	0.03
K	0.00	0.00	0.00	0.00	0.00	0.00	0.00	0.00
Mg#	77	79	77	80	78	94	79	72
P (MPa, P	#REF!	#REF!	#REF!	#REF!	#REF!	#REF!	#REF!	#REF!

	D06R02			D03R01	D03R03	D08R04	D07R01	
rim							core	rim
	52.62	52.85	SiO$_2$	37.41	37.12	37.64	36.44	36.36
	0.41	0.39	TiO$_2$	0.05	0.02	0.00	0.02	0.00
	1.69	1.33	Al$_2$O$_3$	0.00	0.01	0.02	0.00	0.02
	0.00	0.02	Cr$_2$O$_3$	0.00	0.01	0.00	0.00	0.00
	8.87	9.78	FeO*	31.03	30.51	30.31	32.50	34.63
	0.65	0.69	MnO	1.57	1.54	1.52	1.68	1.72
	15.05	15.11	MgO	31.64	32.53	32.09	30.49	28.87
	20.58	20.12	CaO	0.15	0.17	0.18	0.15	0.15
	0.43	0.38	Na$_2$O	0.03	0.00	0.01	0.01	0.01
	0.03	0.02	K$_2$O	0.00	0.00	0.01	0.01	0.02
	100.33	100.69	NiO	0	0	0	0	0.001
			total	101.88	101.91	101.77	101.30	101.77
	6	6	O	4	4	4	4	4
	1.94	1.95	Si	1.00	0.99	1.00	0.99	0.99
	0.01	0.01	Ti	0.00	0.00	0.00	0.00	0.00
	0.07	0.06	Al	0.00	0.00	0.00	0.00	0.00
	0.00	0.00	Cr	0.00	0.00	0.00	0.00	0.00
	0.05	0.05	Fe	0.69	0.68	0.68	0.74	0.79
	0.23	0.26	Mn	0.04	0.03	0.03	0.04	0.04
	0.02	0.02	Mg	1.26	1.29	1.28	1.24	1.18
	0.83	0.83	Ca	0.00	0.00	0.01	0.00	0.00
	0.81	0.80	Na	0.00	0.00	0.00	0.00	0.00
	0.03	0.03	K	0.00	0.00	0.00	0.00	0.00
	0.00	0.00						
	78	76		64	66	65	63	60
	#REF!	#REF!						

R07R05		D06R01	D06R02
core	rim		
36.51	37.15	37.10	37.38
0.01	0.01	0.00	0.00
0.01	0.69	0.01	0.02
0.00	0.02	0.00	0.01
32.52	35.46	31.03	29.18
1.65	1.79	1.41	1.23
30.20	26.52	31.94	33.40
0.15	0.19	0.16	0.17
0.04	0.18	0.00	0.01
0.00	0.16	0.02	0.00
0	0	0	0.002
101.09	102.17	101.67	101.39
4	4	4	4
0.99	1.01	0.99	1.00
0.00	0.00	0.00	0.00
0.00	0.02	0.00	0.00
0.00	0.00	0.00	0.00
0.74	0.81	0.70	0.65
0.04	0.04	0.03	0.03
1.23	1.08	1.28	1.33
0.00	0.01	0.00	0.00
0.00	0.01	0.00	0.00
0.00	0.01	0.00	0.00
62	57	65	67

Sample No	D03R01	D03R03	D08R04	D08R11		D07R01		D07R05
Note				in Cpx and	gm	in Pl rim	gm	
SiO_2	0.10	0.09	0.08	0.09	0.10	0.16	0.13	0.09
TiO_2	10.93	10.53	10.38	11.26	10.95	11.27	12.26	11.90
Al_2O_3	2.81	2.83	2.95	2.61	2.70	2.59	2.07	2.59
Cr_2O_3	0.06	0.00	0.02	0.12	0.00	0.09	0.13	0.06
FeO*	78.09	77.56	78.01	77.77	78.35	75.66	75.54	77.23
MnO	1.05	0.96	1.02	0.94	1.12	0.17	1.10	1.14
MgO	2.81	2.70	2.91	2.68	2.17	2.58	2.08	2.32
CaO	0.03	0.00	0.03	0.03	0.01	0.11	0.03	0.01
Na_2O	0.01	0.00	0.03	0.00	0.05	0.00	0.00	0.00
K_2O	0.04	0.01	0.00	0.02	0.00	0.01	0.10	0.01
total	95.92	94.68	95.44	95.52	95.45	92.64	93.44	95.34
O	4	4	4	4	4	4	4	4
Si	0.00	0.00	0.00	0.00	0.00	0.01	0.00	0.00
Ti	0.29	0.28	0.28	0.30	0.29	0.31	0.34	0.32
Al	0.12	0.12	0.12	0.11	0.11	0.11	0.09	0.11
Cr	0.00	0.00	0.00	0.00	0.00	0.00	0.00	0.00
Fe^{3+}	1.49	1.50	1.50	1.48	1.49	1.46	1.45	1.46
Fe^{2+}	0.82	0.83	0.82	0.83	0.85	0.85	0.85	0.84
Mn	0.03	0.03	0.03	0.03	0.03	0.01	0.03	0.03
Mg	0.15	0.14	0.15	0.14	0.12	0.14	0.11	0.12
Ca	0.00	0.00	0.00	0.00	0.00	0.00	0.00	0.00
Na	0.00	0.00	0.00	0.00	0.00	0.00	0.00	0.00
K	0.00	0.00	0.00	0.00	0.00	0.00	0.00	0.00
XMg-mag	0.060	0.058	0.062	0.058	0.047	0.057	0.047	0.051
TXMg	934	929	940	928	893	926	892	905

D06R01		D06R02	D08R11
core	rim		Crs
0.08	0.07	0.10	98.21
10.49	10.22	9.33	0.143
2.99	2.87	3.19	0.973
0.05	0.06	0.05	0.02
78.10	78.43	77.51	0.066
0.85	0.94	0.84	0.037
2.93	2.31	3.12	0.006
0.00	0.00	0.00	0.014
0.02	0.05	0.00	0.597
0.02	0.04	0.00	0.005
95.52	94.99	94.14	
4	4	4	2
0.00	0.00	0.00	0.99
0.28	0.28	0.25	0.00
0.12	0.12	0.13	0.0115
0.00	0.00	0.00	0.00
1.50	1.50	1.52	0.00
0.82	0.85	0.81	0.00
0.03	0.03	0.03	0.00
0.15	0.12	0.17	0.00
0.00	0.00	0.00	0.00
0.00	0.00	0.00	0.0116
0.00	0.00	0.00	0.00
0.063	0.050	0.067	
941	902	953	

Supplementary Material 1

Dredge assembly used during the cruise YK22-15

During the cruise YK22-15, we used a Satsuki type dredger and depressor-towing body. This assembly is employed to protect the opto-electrical composite cable from any damaging during dredging (Fig. S1). The Satsuki type dredger was connected to the depressor-towing body by a lead wire with 200 m length. The position of the dredger was monitored by a transponder attached to the depressor-towing body (Fig. S2a). The Satsuki type dredger has a size of 800 mm × 740 mm × 120 mm (width, height, and length, respectively) and ~240 kg.
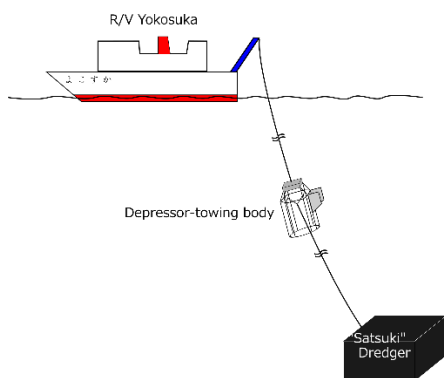

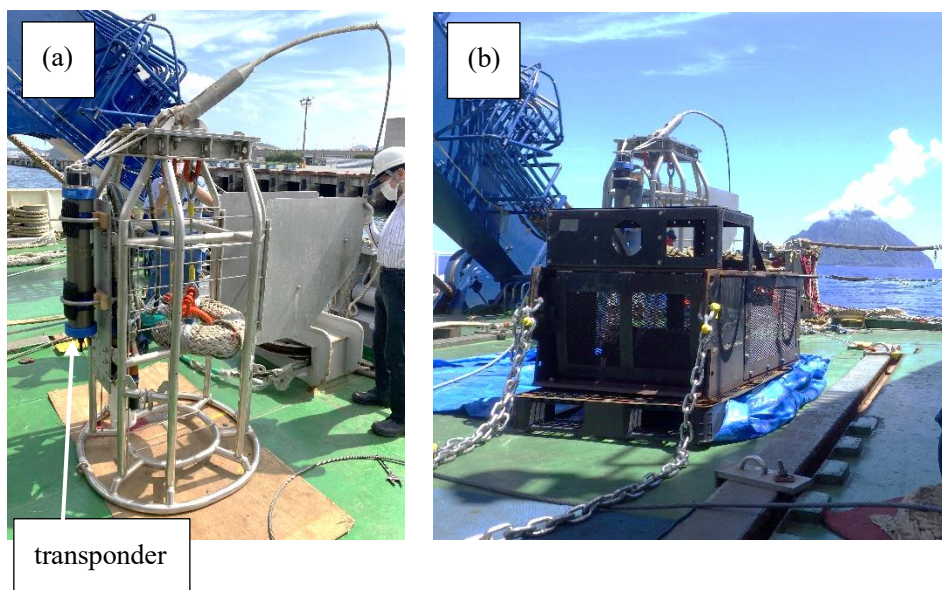Fig. S1. Schematic image of the dredge assembly.

Figure S2. (a) A depressor-towing body equipped with a transponder. (b) Photograph of Satsuki type dredger which is ready for operation.

Table S1. Details of the dredge positions

Dredge number	Hit bottom		Off bottom		Depth (m)[*1]		Tension max. (kN)	Survey time (hh:mm)
	Lat. (SOQ[*1])	Lon. (SOQ[*1])	Lat. (SOQ[*1])	Lon. (SOQ[*1])	On the bottom	Off the Bottom		
D03	24-16.8737N	141-25.6601E	24-16.8458N	141-25.8852E	446	353	41.6	0:36
D04	24-22.0755N	141-26.4721E	24-22.5723N	141-26.4072E	324	299	13.0	0:59
D05	24-18.5790N	141-26.2145E	24-18.6416N	141-26.6848E	369	182	18.1	1:00
D06	24-14.6284N	141-31.1048E	24-15.1767N	141-30.6928E	649	361	16.6	1:12
D07	24-20.6611N	141-31.6256E	24-20.3546N	141-31.0876E	525	256	28.1	1:17
D08	24-16.8088N	141-26.0734E	24-16.6746N	141-26.5212E	383	294	17.3	1:02

*SOQ = SGK Transponder's position

*SOJ = Ship's position

Table S2. Trace element analysis of secondary standard (JB-2) and the reference value

Sample	JB-2, meas	JB-2, reference* (μg/g)
Sc	51.728	54.08
Co	34.64	37.57
Ni	12.417	14.77
Cu	209.443	222.1
Rb	5.732	6.4
Sr	175.628	178.2
Y	21.115	23.56
Zr	43.894	48.25
Nb	0.439	0.565
Cs	0.754	0.8
Ba	208.065	218.1
La	2.131	2.281
Ce	6.297	6.552
Pr	1.096	1.129
Nd	6.168	6.392
Sm	2.208	2.266
Eu	0.792	0.836
Gd	3.15	3.123
Tb	0.572	0.5863
Dy	3.915	3.868
Ho	0.854	0.863
Er	2.584	2.537
Tm	0.376	0.393
Yb	2.525	2.529
Lu	0.382	0.3894
Hf	1.49	1.487
Ta	0.032	0.0396
Tl	0.036	0.034
Pb	4.963	5.25
Th	0.252	0.2576
U	0.155	0.1528

*Reference of JB-2 is taken from GeoReM database
(Jochum et al. Geostand. Geoanal. Res. 40, 333-350, 2016)